Crystallographic characters of 11¯22 twin-twin junctions in titanium

Shun Xu, Mingyu Gong, Xinyan Xie, Yue Liu, Christophe Schuman, J.S. Lecomte, Jian Wang

Crystallographic characters of $\{11\bar{2}2\}$ twin-twin junctions in titanium

Shun Xu[a,b,c], Mingyu Gong[c], Xinyan Xie[c], Yue Liu[d], Christophe Schuman[a,b],Jean-Sébastien Lecomte[a,b] and Jian Wang[c]

[a]Laboratoire d'Etude des Microstructures et de Mécanique des Matériaux (LEM3), CNRS UMR 7239, Université de Lorraine, Metz, France;

[b]Laboratory of Excellence on Design of Alloy Metals for low-mAss Structures (DAMAS), Université de Lorraine, Metz, France;

[c]Mechanical and Materials Engineering, University of Nebraska-Lincoln, Lincoln, NE, USA;

[d]State Key Lab of Metal Matrix Composites, School of Materials Science and Engineering, Shanghai Jiao Tong University, Shanghai, P.R. China

CONTACT Jian Wang jianwang@unl.edu

ABSTRACT

$\{11\bar{2}2\}$ contraction twins that are commonly activated in α-titanium interact to each other and form three types of twin–twin junctions ($C^I_{i,j+1}$, $C^I_{i,j+2}$, $C^I_{i,j+3}$TTJs) corresponding to the crystallography of six twin variants C^I_i (i = 1,2, … , 6). We detected 243 $\{11\bar{2}2\}$ TTJs in rolled pure α-titanium sheets. Electron backscatter diffraction analysis reveals that $C^I_{i,j+1}$ TTJs are profuse, 79.8% among three types while $C^I_{i,j+2}$, and $C^I_{i,j+3}$TTJs take up 17.7 and 2.5%. Twin transmission does not occur. Consequently, boundaries associated with twin–twin interactions block twin propagation and influence twin growth. We explain structural features of TTJs according to the Schmid factor analysis and the reaction mechanism of twinning dislocations. The knowledge regarding TTJs provides insight for improving the predictive capability of meso/macro-scale crystal plasticity models for hexagonal metals.

KEYWORDS: Twin; dislocation; titanium; electron backscatter diffraction

1. Introduction

Titanium (Ti) and its alloys attract wide application in aerospace, chemical industry and medical implants due to their excellent physical and mechanical properties, such as high strength, excellent corrosion resistance and good biocompatibility [1]. Owing to its hexagonal close packed structure, α-Ti plastically deforms via slipping and twinning. Twinning is a major deformation mode that accommodates strains along the c-axis. A tremendous amount of experimental work has been carried out for α-Ti and other hexagonal metals to understand mechanisms and mechanics of slips and twins in the context of temperatures and strain rates

[2,3], cyclic loading [4–6], strain path changes [7], textures [8,9], twinning modes [10], grain size effects [11,12] and sample size effects [13,14]. Sinha et al. [15] studied the effect of initial orientation on deformation behaviours of polycrystalline titanium, indicating the dependence of strength and strain hardening rate on the initial orientations. Gurao et al. [16] studied the microstructure and texture evolution of commercially pure titanium with four different initial orientations subjected to compression at various strain rates. The results revealed that plastic deformation of α-Ti at high strain rate (1.5×10^3 s^{-1}), compared to low strain rate (3×10^{-4} s^{-1}), is characterised by extensive twinning. For the samples with different orientations, the differences in the strain hardening response are reduced at high strain rate. At room temperature, $\{10\bar{1}2\}\langle\bar{1}011\rangle$ extension twinning and $\{11\bar{2}2\}\langle11\bar{2}\bar{3}\rangle$contraction twinning are commonly observed [17–19]. Other twinning modes, $\{11\bar{2}1\}\langle\bar{1}\bar{1}26\rangle$, [20-23], $\{11\bar{2}4\}\langle22\bar{4}\bar{3}\rangle$ [24–26] and $\{10\bar{1}1\}\langle10\bar{1}\bar{2}\rangle$ [27], are rarely activated and strongly depend on temperature and loading condition. $\{11\bar{2}2\}$ contraction twins in α-Ti are frequently generated in rolled pure titanium under compression along the normal direction (ND) [28], under rolling [29], under tension along the rolling direction (RD) [30] and under monotonic simple shear tests [31]. Serra et al. [32] identified twinning dislocations associated with $\{11\bar{2}2\}\langle11\bar{2}\bar{3}\rangle$ contraction twins in α-Ti, which has step character with a unit height of three atomic layers and the Burgers vector of $\lambda\langle11\bar{2}\bar{3}\rangle$. λ equals to $\frac{k^2-2}{3(k^2+1)}$, and k is the c/a ratio. Morrow et al. [33] characterised $\{11\bar{2}2\}\langle11\bar{2}\bar{3}\rangle$ twin boundaries and found steps/facets associated with the pileup of twinning dislocations along the basal plane. Salem et al. [18,34] investigated the role of deformation twinning in strain hardening of polycrystalline titanium, and found that the second stage of strain hardening curve is attributed to $\{11\bar{2}2\}$ twinning. In addition, Double twinning, i.e. secondary $\{10\bar{1}2\}$ extension twin in primary $\{11\bar{2}2\}$ contraction twin, commonly occurs in α-Ti [29,35].

When two twin variants interact to each other, forming twin–twin junction (TTJ). Recent study of $\{10\bar{1}2\}\}$ twin–twin interactions in Mg and Mg alloys [36] revealed that one twin does not transmit into the other twin. Consequently, twin–twin boundaries (TTB) form as a result of the reaction of twinning dislocations. TTBs hinder the motion of twinning dislocations toward the TTB, resulting in strain hardening during twinning. Atomistic simulations [37] and TEM characterisation [38] further examine the characters of TTBs that are identified according to crystallography and electron backscatter diffraction (EBSD) analysis [36]. However, $\{11\bar{2}2\}$ twin–twin junctions were not studied. The contribution of $\{11\bar{2}2\}$ twin–twin junctions (TTJs) to the strain hardening was thus not considered in theoretical models and simulations.

In this work, we conduct statistical analysis of $\{11\bar{2}2\}$ TTJs. There are three types of $\{1\bar{1}22\}$ TTJs according to the crystallography of $\{11\bar{2}2\}$ twins. EBSD analysis shows that one type of TTJs is frequently activated while the other two are less observed. Twin transmission does not happen. We characterise structures of boundaries associated with twin–twin interactions according to crystallographic, EBSD analysis and dislocation theory. Structural features of TTBs are then explained according to the Schmid factor analysis and the reaction mechanism of twinning dislocations. The knowledge regarding TTJs provides insight for improving the predictive capability of meso/macro-scale crystal plasticity models for hexagonal metals.

2. Crystallography of twin–twin interactions

Figure 1a shows a hexagonal closed pack structure. Six equivalent $\{11\bar{2}2\}$ twin variants are denoted by C_i^I (i = 1,2, … , 6). The superscript I refers to type I contraction twin, and the subscript i increases by a counter-clockwise rotation around the *c*-axis. When one twin meets another twin, TTBs form. The boundary plane is geometrically determined as the bisection plane of the two twin planes [36,39]. Interactions of two $\{11\bar{2}2\}$ twin variants are classified into three types and summarised in Figure 1 and Table 1.

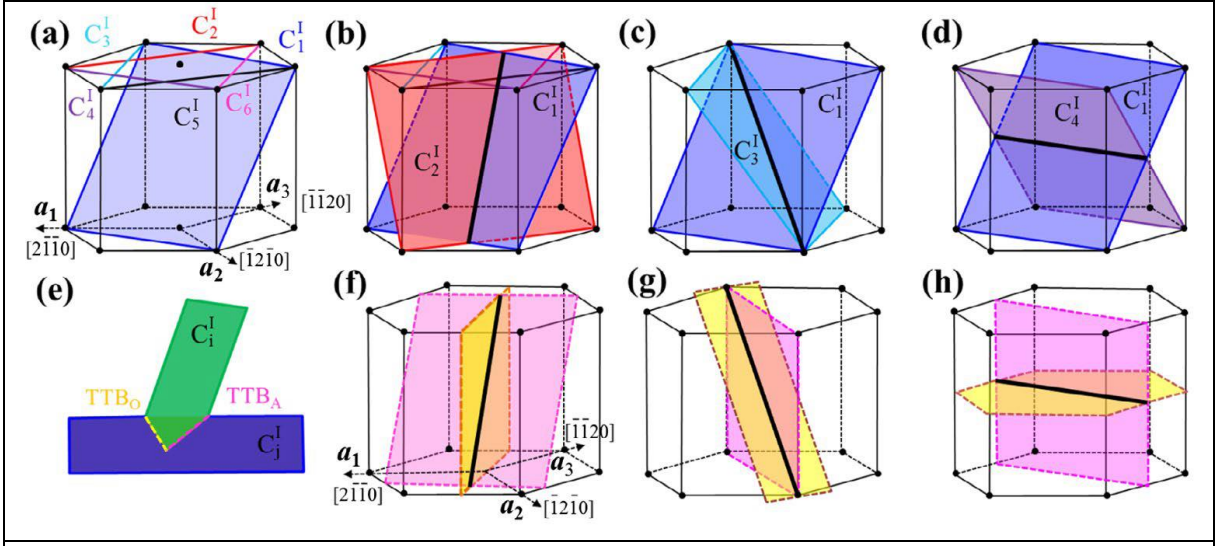

Figure 1. (a) Six $\{11\bar{2}2\}\langle 11\bar{2}\bar{3}\rangle$ (C_i^I) twin variants form three types of twin–twin junctions. (b) Type I $C_{i,j+1}^I$with the intersection line along $[0\bar{2}23]$; (c) Type II $C_{i,j+2}^I$ with the intersection line along $[2\bar{4}23]$; (d) Type III $C_{i,j+3}^I$ with the intersection line along $[1\bar{1}00]$. The bold solid lines indicate the intersection line. (e) Schematic of twin–twin boundaries associated with TTJ, where TTB_A (marked by purple) and TTB_O (marked by yellow) are formed on the acute side and on the obtuse side, respectively.

Table 1. Crystallographic characters of three types of $\{11\bar{2}2\}$twin–twin junctions.

TTJs	Intersection line	TTB_A			TTB_O		
		In matrix	In C_1^I	In C_i^I (i=2…4)	In matrix	In C_1^I	In C_i^I (i=2…4)
$C_{i,i+1}^I$	$[0\bar{2}23]$	$(03\bar{3}4)$	$(232\bar{2}\bar{5}18)$	$(\bar{2}32\bar{5}\bar{2}18)$	$(\bar{2}110)$	$(9\bar{1}2\bar{3}10)$	$(93\bar{1}\bar{2}10)$
			Twist 58.29°			Twist 0.17°	
$C_{i,i+2}^I$	$[2\bar{4}23]$	$(\bar{1}010)$	$(2\bar{5}3\bar{1}0)$	$(\bar{3}5\bar{2}10)$	$(\bar{1}2\bar{1}4)$	$(58\bar{3}\bar{5}\bar{5}6)$	$(\bar{5}\bar{5}\bar{3}58\bar{6})$
			Twist 0.24°			Twist 77.02°	
$C_{i,i+3}^I$	$[1\bar{1}00]$	$(\bar{1}\bar{1}20)$	$(\bar{3}\bar{3}6\bar{2}0)$	$(\bar{3}\bar{3}620)$	(0002)	$(22\bar{4}3)$	$(\bar{2}2\bar{4}\bar{3})$
			Twist 0°			Twist 0°	

Type I is the interaction of C_i^I and C_{i+1}^I variants (referred to as $C_{i,j+1}^I$). The intersection line l_{12} of the two twin planes is along $[0\bar{2}23]$. Type II is the interaction of C_i^I and C_{i+2}^I variants (referred to as $C_{i,j+2}^I$). The intersection line l_{13} of the two twin planes is along $[2\bar{4}23]$. Type III is the interaction of C_i^I and C_{i+3}^I variants (referred to as $C_{i,j+3}^I$). The intersection line l_{14} between the two twin planes is along $[1\bar{1}00]$.

Figure 1f–h show bisection planes (i.e. TTBs) associated with three TTJs. The TTB in the acute side of the two twinning planes is referred to as TTBA (marked in pink) while the other in the obtuse side as TTB_O (marked in yellow) as depicted in Figure 1e. For type I TTJs, TTBA bonds the $(232\overline{2}518)$plane of the C_1^I twin and the $(\overline{23}\,25\,\bar{2}\,18)$plane of the C_2^I twin, and is parallel to the $(03\bar{3}4)$plane of the matrix. The interplanar spacing of $(232\overline{2}518)$- plane is 0.010 nm for Ti. TTB_O bonds the $(9\,\overline{12}\,3\,\overline{10})$ plane of the C_1^I twin and the $(93\overline{12}10)$ plane of the C_2^I twin, and is parallel to the $(\bar{2}110)$ of the matrix. The interplanar spacing of $(93\overline{12}10)$ is 0.021 nm for Ti. In addition, the $(232\overline{2}518)$ plane is twisted 58.29° relative to $(\overline{23}25\,\bar{2}18)$ plane about their normal, and the $(9\overline{12}3\overline{10})$ plane is twisted 0.17° relative to the $(93\overline{12}10)$ about their normal. From the geometry point of view, the TTB_O interface might have lower formation energy than the TTB_A interface because of its high areal density and small twist angle. Wang et al. systematically studied symmetrical tilt grain boundaries in α-Ti using atomistic simulations with empirical interatomic potentials [40,41] and found that the equilibrium TTB_O interface has low formation energy of 710 mJ/m^2 while the equilibrium TTB_A interface has high formation energy of 820 mJ/m^2 [40]. For Type II TTJs, TTB_A bonds the $(2\bar{5}3\overline{10})$ plane of the C_1^I twin and the $(\bar{3}5\bar{2}10)$ plane of the C_3^I twin, and is parallel to the $(\bar{1}010)$ plane of the matrix. The interplanar spacing of $(2\,\bar{5}\,3\,\overline{10})$ plane is 0.037 nm. TTB_O bonds the $(2\bar{5}3\overline{10})$ plane of the C_1^I twin and the $(\overline{55}\,\bar{3}\,5\,8\,\bar{6})$ plane of the C_3^I twin, and is parallel to the $(\bar{1}2\,\bar{1}4)$ plane in the matrix. The interplanar spacing of $(\overline{55}\,\bar{3}\,5\,8\,\bar{6})$ is 0.005 nm. In addition, the two $(2\bar{5}3\overline{10})$ planes are relatively twisted 0.24° about their normal, and the two $\{\overline{55}\,\bar{3}\,5\,8\,\bar{6}\}$ planes are relatively twisted 77.02° about their normal. Thus, the TTB_A interface might have lower formation energy. For Type III TTJs, the intersection line is parallel to their zone axis, and the two TTBs are symmetrical tilt boundary. TTB_A bonds the $(\bar{3}\,\bar{3}\,6\,\overline{20})$plane of the C_1^Itwin and the $(\bar{3}\,\bar{3}\,6\,20)$ plane of the C_4^I twin, and is parallel to the $(\bar{1}\bar{1}20)$ plane in the matrix. The interplanar spacing of $^-(\bar{3}\,\bar{3}\,6\,20)$ plane is 0.021 nm. TTB_O bonds the $(\bar{2}\,\bar{2}\,4\,3)$ plane of the C_3^I twin and the $(\bar{2}\,\bar{2}\,4\,\bar{3})$ plane of the C_4^I twin, and is parallel to the (0002) plane of the matrix. The interplanar spacing of $22\bar{4}3$- plane is 0.034 nm. However, these non-equilibrium and equilibrium TTB_A and TTB_O interfaces associated with twin–twin interactions were not studied using atomistic simulations [42].

3. Experiments

The rolled commercially pure titanium T40 sheet (ASTM grade 2) with a thickness of 1.5 mm was annealed in a vacuum furnace at 800°C for 2 h. The annealed sheet was then compressed along the normal direction at a strain rate 1.0e^{-3} s^{-1} at room temperature using a Zwick 120T machine. After compression, the surface of the deformed sample was ground with SiC papers of grits from 1200# to 4000#. Electrolytic polishing was performed using a solution of 10% perchloric acid and 90% methanol at 35 V for 5 s at 5 °C. EBSD measurements were conducted in a JEOL JSM-6500F field emission gun scanning electron microscopy equipped with an EBSD camera and the AZtec acquisition software package (Oxford Instruments).

Figure 2a shows one typical EBSD pattern of the polished surface with a step size of 0.5 μm. Corresponding to the crystallography of twins in α-Ti, twin variants are identified according to their misorientation: $\{11\bar{2}2\}$ contraction twins are rotated ~64° around $\langle1\bar{1}\,00\rangle$; $\{10\bar{1}2\}$ extension twins are rotated ~87° around $\langle11\bar{2}\,0\rangle$; $\{11\bar{2}1\}$ } extension twins are rotated ~35°

around $\langle 1\bar{1}\ 00\rangle$. Correspondingly, we identified twin variants, double twins ($\{10\bar{1}2\}$ extension twins in $\{11\bar{2}2\}$ contraction twins), and $\{11\bar{2}2\}$ TTJs. The transmission of one twin crossing another twin was not observed. The intriguing feature associated with TTJs is that TTB only forms in one side of the incoming twin. The details will be discussed in the following sections. We detected 243 TTJs according to EBSD patterns in a 4*8 mm2 surface of the deformed sample. Figure 2b shows their frequency. Type I TTJs account for 79.8%, Type II TTJs and Type III TTJs take up 17.7 and 2.5%, respectively. In order to further explore the dependence of TTJ Types on stresses, we calculated the SFs associated with these twins according to the stresses in their parent grains and statistically grouped them according to the order of their SFs (Figure 2c). SF_{ij} (i, j = 1 … 6) indicates the rank of the SFs associated with the two twins. For example, SF23 means that one twin variant has the second highest SF and the other twin variant has the third highest SF. The interesting finding is that the SFs of two twins associated with 93% TTJs are first, second or third highest among six variants. Such information enables us to explore the frequency of each type of TTJs.

TTBs form as two twins meet. In order to characterise structural feature of TTBs and TTJs, here we describe a geometrical analysis method based on traces of boundary planes on the observed surface and corresponding pole figures. Because the normal of the observed surface is along an arbitrary crystallographic direction, we firstly define the trace of a boundary plane on the observed surface according to EBSD data, then we use the corresponding pole figure to determine which crystallographic plane is a best fit for the trace. As shown in Figure 2d, two planes P_i (h_i k_i i_i l_i) and P_j (h_j k_j i_j l_j) intersect. The angle θ_{ij} between the two planes is calculated by

$$\theta_{ij} = \cos^{-1}\left(\frac{h_i h_j + k_i k_j + \frac{1}{2}\left(h_i k_j + h_j k_i\right) + \frac{3a^2}{4c^2} l_i l_j}{\sqrt{\left(h_i^2 + k_i^2 + h_i k_i + \frac{3a^2}{4c^2} l_i^2\right)\left(h_j^2 + k_j^2 + h_j k_j + \frac{3a^2}{4c^2} l_j^2\right)}}\right) \quad (1)$$

However, the measured angle between the traces of the two planes on an observed surface varies with respect to the normal of the observed surface. On an observed surface P_o (h_o k_o i_o l_o), the trace of P_i on P_o is given by

$$l_{io} = \left[\frac{a}{c} k_i l_o - \frac{a}{c} k_o l_i,\ \frac{\sqrt{3}a}{3c} l_i\left(2h_o + k_o\right) - \frac{\sqrt{3}a}{3c} l_o\left(2h_i + k_i\right),\ \frac{2\sqrt{3}a}{3c} h_i k_o - \frac{2\sqrt{3}a}{3c} h_o k_i\right] \quad (2)$$

and the trace of P_j on P_o is given by

$$l_{jo} = \left[\frac{a}{c} k_j l_o - \frac{a}{c} k_o l_j,\ \frac{\sqrt{3}a}{3c} l_j\left(2h_o + k_o\right) - \frac{\sqrt{3}a}{3c} l_c\left(2h_j + k_j\right),\ \frac{2\sqrt{3}a}{3c} h_j k_o - \frac{2\sqrt{3}a}{3c} h_o k_j\right] \quad (3)$$

The angle $\theta_{ij,o}$ between the two traces is given by

$$\theta_{ij,o} = \cos^{-1}\left(\frac{l_{io} \cdot l_{jo}}{|l_{io}||l_{jo}|}\right) \quad (4)$$

The angle $\theta_{ij,o}$ represents the measured angle between the two planes P_i and P_j on the observed surface P_o. As illustrated in Figure 2e, the pole figure has Y ‖ the intersection line between the observed surface and (0 0 0 2) plane, Z ‖ the normal of the observed plane, and X = Y × Z. For two twin planes P_1 $(11\bar{2}2)$ and P_4 $(\bar{1}\bar{1}22)$in Ti, the angle θ_{14} is 64°. When the observed surface P_o is (0002) plane, the red lines indicate the traces of the two planes on the observed surface and are parallel. Thus, the measured angle $\theta_{14,o}$ is equal to 0°. When P_o is $(1\bar{1}02)$, $\theta_{14,o}$ = 46°. The blue dashed lines indicate the traces of the two planes on the observed surface. Using this method, we identify twin–twin boundaries.

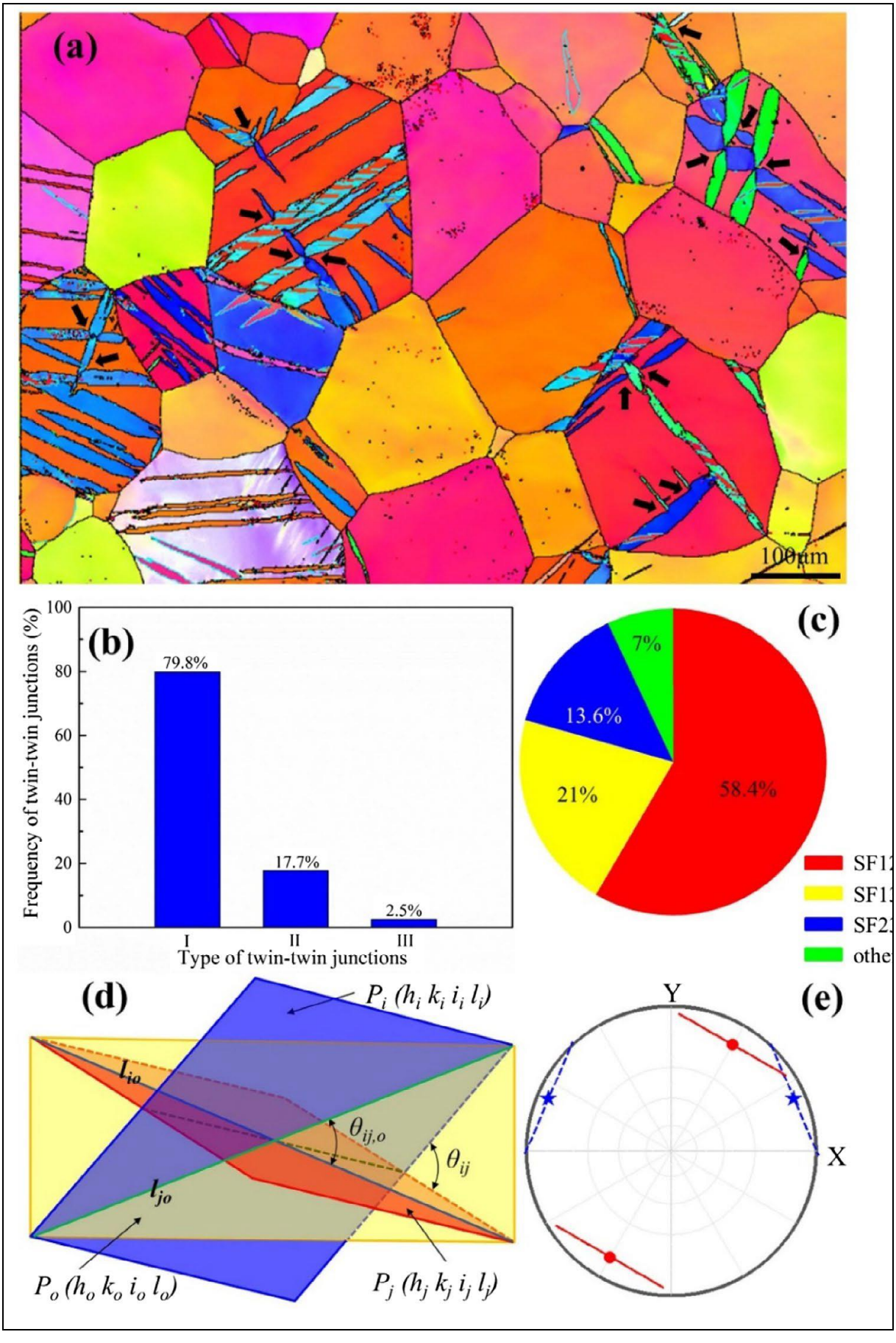
(a)
100μm
(b)
Frequency of twin-twin junctions (%)
100
80
60
40
20
0
79.8%
17.7%
2.5%
I
II
III
Type of twin-twin junctions
(c)
7%
13.6%
21%
58.4%
SF1
SF1
SF2
othe
(d)
P_i (h_i k_i i_i l_i)
l_{io}
$\theta_{ij,o}$
θ_{ij}
l_{jo}
P_o (h_o k_o i_o l_o)
P_j (h_j k_j i_j l_j)
(e)
Y
X

Figure 2. (a) A typical EBSD map of deformed sample showing twin–twin junctions (indicated by the black arrows). (b) Statistic plot of frequency of 243 detected twin–twin junctions; (c) Statistic plot of Schmid factors associated with twin–twin junctions. The subscripts ij of SF_{ij} (i, j = 1 … 6) mean the rank of the Schmid factors associated with the two intersected twins. (d) Schematic of the angle between two twin planes of twins C_i^I and C_j^I on an observed plane P_o. (e) A pole figure showing the traces of two twin planes on the observed plane. The red symbols correspond to the observed plane P_o = (0002), and the blue symbols correspond to the observed plane $P_o = (\bar{1}\bar{1}02)$.

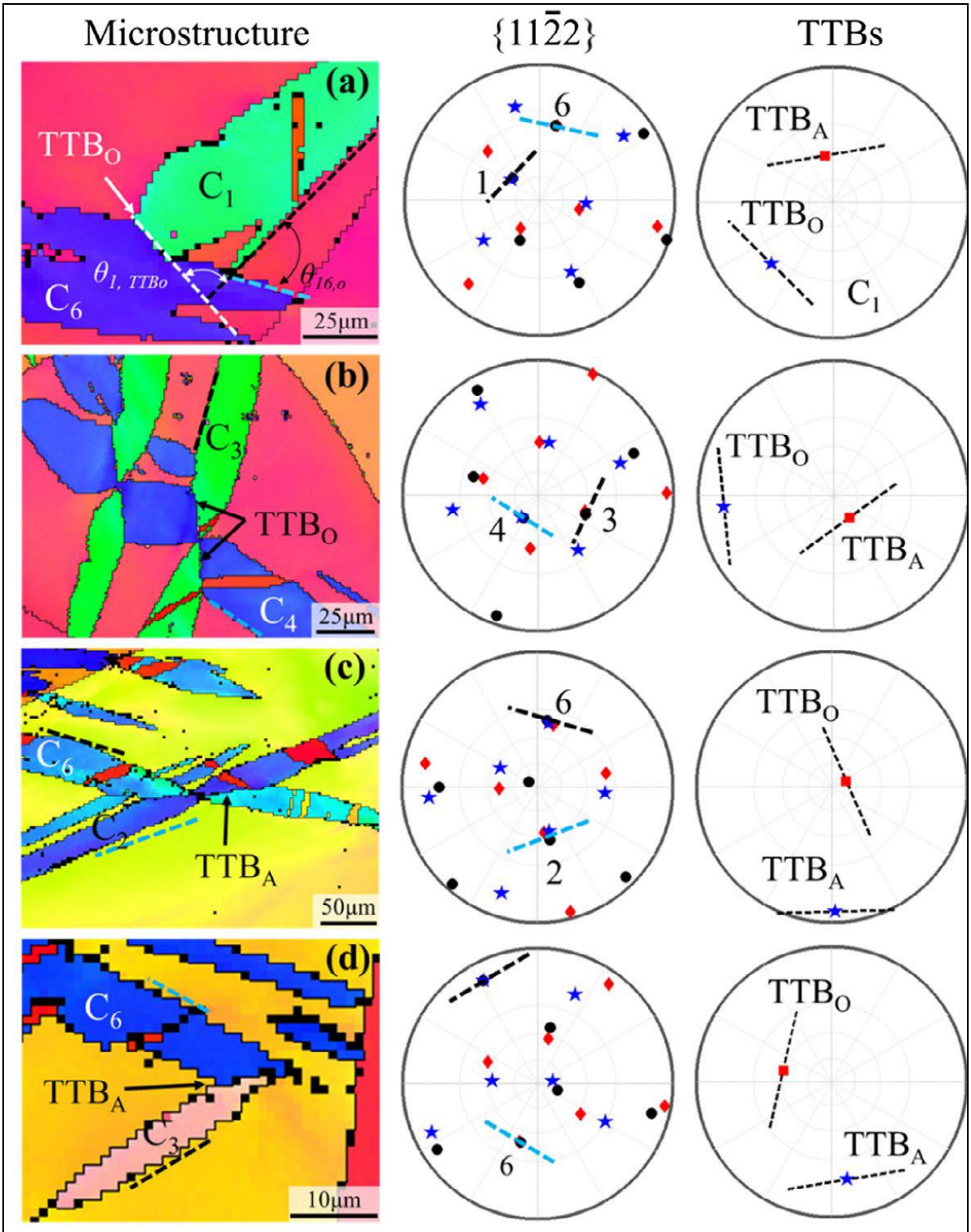

Figure 3. Microstructure of twin–twin junctions and their corresponding pole figures. (a) (b) Type I, (c) Type II, (d) Type III. The trace of the twinning planes drawn in the pole figures of {11$\bar{2}$2} planes. The traces of TTB_A and TTB_O associated with the TTJ were shown in the pole figures of TTBs.

For Type I TTJs, Figure 3a shows a $C_{1,6}^{I}$ TTJ, i.e $(11\bar{2}2)[11\bar{2}\bar{3}]$ (C_1^I) and $(2\bar{1}\ \bar{1}\ 2)[2\bar{1}\ \bar{1}\bar{3}]$ (C_6^I) twins. Crystallographic planes of TTBA and TTBo are parallel to $(30\bar{3}4)$ and $(1\bar{2}10)$ planes of the matrix, respectively. From the pole figure, we determine the traces of C_1^I and C_6^I twin planes, and the traces of $(30\bar{3}4)$and $(1\bar{2}10)$planes of the matrix. The angle $\theta_{16,O}$ between C_1^I and C_6^I twin planes on the observed surface Po (0.2634, 1.2028, 1.4662, 3.9714) is 64°, which is approximately equal to the measured angle 63.25° as indicated by black arrows in the EBSD image (Figure 3a).In addition, the angle $1TTB_o$ between the traces of C_1^I and the TTB_O plane $(1\bar{2}10)$ is 81.33°,which is close to the measured angle 81.98° according to the EBSD image. Thus, TTB_O forms as predicted by the crystallography of the TTJ. However, TTBA does not form. Another example in Figure 3b is associated with the $C_{3,4}^{I}$TTJ, i.e. $(2\bar{1}\ \bar{1}\ 2)[2\bar{1}\ \bar{1}\bar{3}]$ (C_3^I) and $(11\bar{2}2)[11\bar{2}\bar{3}]$ (C_4^I) twins on the observed plane Po (1.1206, 0.6045, 1.7251, 3.7693). TTB_A and TTB_o are parallel to $(30\bar{3}4)$ and$(1\bar{2}10)$ planes of the matrix, respectively. The angle $\theta_{3,TTBo}$ between C_3^I twin plane and the TTBO plane on this observed plane is 27°, which is close to the measured angle 26.5° according to the EBSD image. Again, TTB_A is not observed. It is worth mentioning that TTB_o forms in all type I TTJs while TTB_A does not form.or Type II TTJs, Figure 3c shows a $C_{2,6}^{I}$TTJ which is associated with $(11\bar{2}2)[11\bar{2}\bar{3}]$ and $(2\bar{1}\ \bar{1}\ 2)[2\bar{1}\ \bar{1}\bar{3}]$ twins. On the observed plane (0.9163, 1.3495, 2.2658, 2.9724), TTBA forms while TTBO does not form. Among all type II TTJs, we only observed TTBA. Type III TTJs are rarely observed in the EBSD data. Figure 3d shows a Type III TTJ that consists of $(2\bar{1}\ \bar{1}\ 2)[2\bar{1}\ \bar{1}\bar{3}]$ (C_3^I) twin and $(2\bar{1}\ \bar{1}\ 2)[2\bar{1}\ \bar{1}\bar{3}]$ (C_6^I) twin. On the observed planes (0.8609, 1.8936, 1.0327,3.5874), we only observed TTB_A.

4. Discussions

EBSD analysis reveals so far that type I TTJs are the most popular among three types of TTJs, twin transmission does not occur and TTBs only form in the one side of the incoming twin. We address these structural features according to stresses and dislocation structures of boundaries.

4.1. High frequency of type I TTJs

According to the SF analysis for detected TTJs, twin variants are activated when their SFs are the first three highest among six variants. Without loss of generality, we conduct a generalised Schmid factor (SF) analysis. $\{11\bar{2}2\}$ twin variant CI1 is chosen in this study. The grain is subjected to uniaxial compression. We determine the loading domain in which the activated twin has the first, second or third highest SF among six variants. Figure 4a shows the CI1 loading domain in which the SF associated with C_1^I is the first, second or third highest among six twin variants. The similar analysis is conducted for twin variants C_2^I, C_3^I, and C_4^I, as plotted in Figure 4b–d, respectively. For a pair of twins that form a TTJ, the common loading domain is determined by overlapping their loading domains. Figure 4e–g show the common loading domain associated with three types of TTJs. It is noticed that type I TTJ will be activated with high SFs under most loadings in the common loading domain, while type III TTJ will be activated with smallest SFs in the common loading domain. Therefore, under compression along the normal direction of rolling Ti sheets with a strong texture (Figure 4h), Type I TTJs

will be profusely activated while Type III TTJs will be rarely activated. This is consistent with experimental observation.

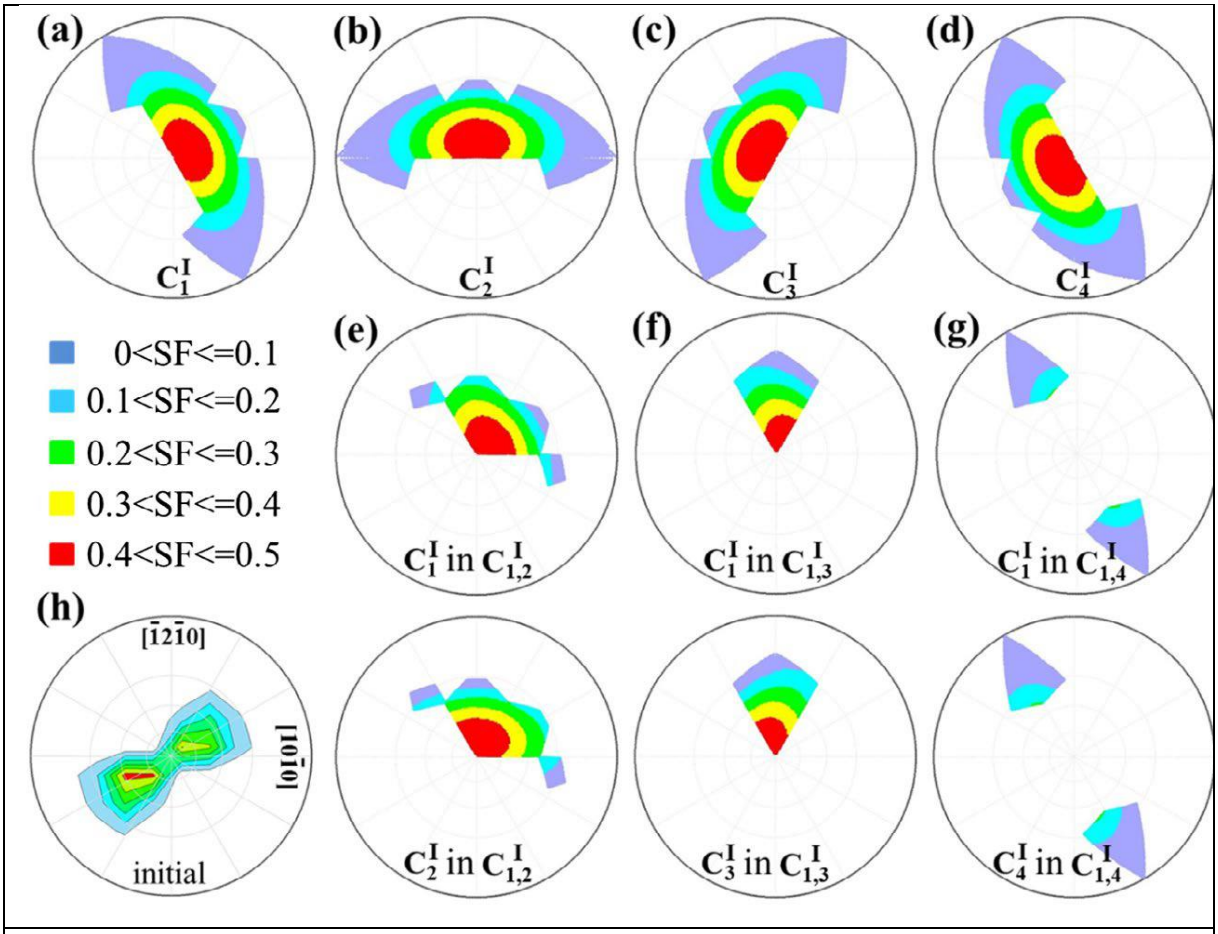

Figure 4. Loading domains associated with formation of TT Js, showing Schmid factors of (a) C_1^I, (b) C_2^I, (c) C_3^I, and (d) C_4^I when the parent crystal is subjected to uniaxial compression. The common loading domains associated with the formation of TT Js (e) C_1^I and C_2^I in $C_{1,2}^I$, (f) C_1^I and C_3^I in $C_{1,3}^I$ and (g) C_1^I and C_4^I in $C_{1,4}^I$. (h)Inverse pole figure of the initial grains.

4.2. Twin transmission

A general analysis for identifying the possibilities of a twin crossing the other twin can be done using the Schmid criterion [36]. To facilitate this discussion, we refer to the pre-existing twin as CI1 and the incoming twin as CIj (j = 2,3,4,5,6). Taking the twin pair C_1^I and C_4^I as an example, Figure 5a and b plot the Schmid factor (SF) associated with the two twin variants in an inverse pole figure when the parent crystal is subjected to uniaxial compression. A positive SF (red domain) is associated with the stress directions that induce a resolved shear along the positive shear direction and activate C_i^I twinning. The domain with zero SF is depicted in white and with negative SF in blue. The loading domain in which two twins can be activated is defined as the common loading domain, which is the overlap red region (the outline of the colour region in Figure 5c) by overlapping Figure 5a and b. In the common loading region, we recalculated the SF associated with the twin C_4^I in the twinned crystal C_1^I. The SF of CI4 inside C_1^I twin is plotted in Figure 5c. It seems that twin transmission is possible because the

red region is part of the common loading domain. However, Figure 4g reveals the formation of the $C_{1,4}^{I}$TTJ in the small loading domain. When refining the loading domain according to Figure 5g, it is obvious that the common loading domain associated with the transmission of C_4^I into C_1^I twin has very small SF (Figure 5d). Thus, twin transmission is mechanically unfavourable. Using the same analysis, we examine the feasibility of twin transmission associated with other four twin variants C_2^I, C_3^I, C_5^I, and C_6^I as shown in Figure 5e–h. The outline of the colour region shows the common loading domain associated with the positive SFs for both twins in the parent disregarding the formation of $C_{i,j}^{I}$TTJs, while the dashed line further refines the common loading domain. It is clear that twin transmission is mechanically unfavoured because of the near zero or negative SF associated with the transmitted twin in the pre-existing twin. This is in agreement with the experimental results.

4.3. Dislocation structures of TTBs.

The formation of TTBs was described as the reaction of twinning dislocations (TDs) [36].

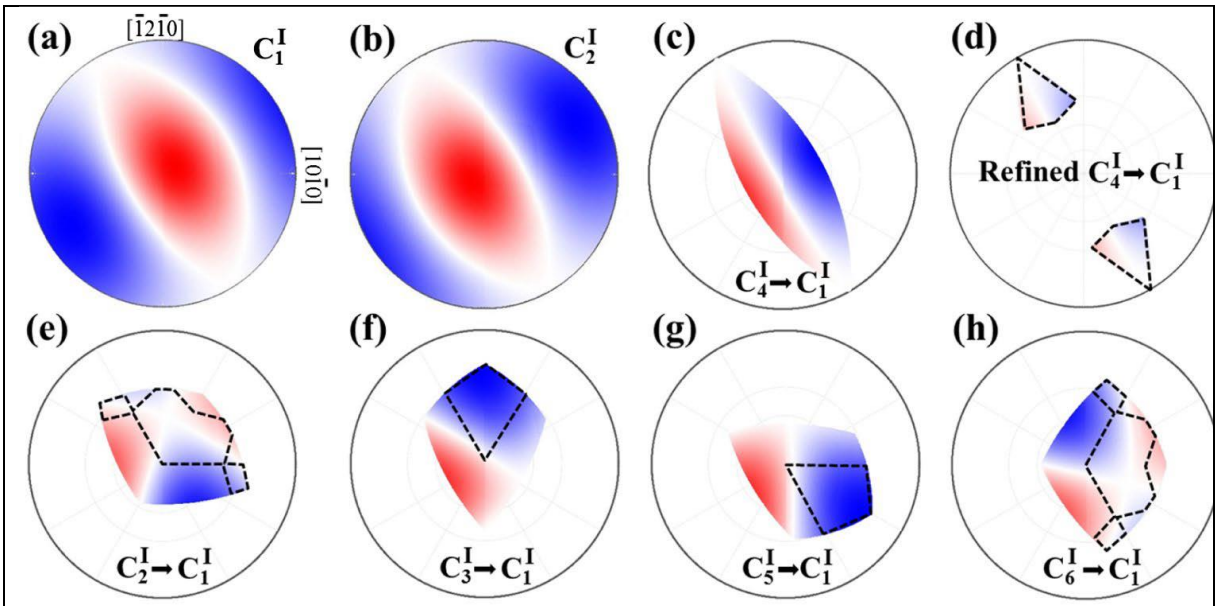

Figure 5. The feasibility analysis of twin transmission according to Schmid factors (SF) of twin variants, when the parent crystal is subjected to uniaxial compression. (a) and (b) the loading domain associated with the activation of C_1^I and C_4^I in the parent crystal. (c) The SF associated with C_4^I twin variant in the twinned crystal C_1^I when the crystal is subjected to the loading in the common loading domain. (d) The refined common loading domain according to the feasibility of $C_{1,4}^{I}$TT J's formation. Red indicates domain with positive SF while blue with negative SF. The common loading domain (colour region) and the refined common loading domain (outlined by the dashed line) associated with twin transmission of (e) C_2^I, (f) C_3^I, (g) C_{25}^I and (h) C_6^I twin variant into the twinned domain C_i^I

When two intersected twins grow through the glide of TDs, these TDs meet and react, forming TTBs. Therefore, the Burgers vector of the resultant dislocations at the TTB is the sum of the TDs associated with the two twins, where all dislocation lines are assumed along the intersection line. For TTB_A associated with $C^I_{1,2}$TTJ, the Burgers vector of the resultant interface dislocation is$b_t^{C_2^I} + b_t^{C_2^I} \Longrightarrow b_{21}^A$. Correspondingly,

$$\lambda[1\bar{2}13] + \lambda[\bar{1}\bar{1}23] = 3\lambda[0\bar{1}12] \quad (5)$$

The Burgers vector of the resultant interface dislocation in TTB_O is thus equal to $b_t^{C_2^I} - b_t^{C_2^I} \Longrightarrow b_{21}^O$. Correspondingly,

$$\lambda[1\bar{2}13] + \lambda[\bar{1}\bar{1}23] = \lambda[2\bar{1}10] \quad (6)$$

Where $\lambda = \frac{k^2-2}{3(k^2+1)}$, 0.0491 for titanium. $b_t^{C_2^I}$t is the Burgers vector of the TD associated with C_2^I twinning. b_{21}^A and b_{21}^O represent the Burgers vectors of the resultant boundary dislocations on the acute side and obtuse side, when C_2^I twin meets primary C_1^I twin. We also analyse other two twin–twin interactions, C_3^I twin meets CI1 twin and C twin meets C_1^Itwin. The resultant interface dislocations have Burgers vectors: $b_{31}^A = 3\lambda[10\bar{1}0]$, $b_{31}^O = \lambda[1\bar{2}16]$, $b_{41}^A = 2\lambda[11\bar{2}0]$, $b_{41}^0 = 6\lambda[0001]$The elastic energy of these dislocations is proportional to the square of the magnitude of their Burgers vectors. According to the Frank's law [43], the elastic energy of two TDs associated with C_2^I and C_1^Itwins is proportional to 63.36(λa)^2. The elastic energy for a resultant interface dislocation in TTBs is proportional to 117.72(λa)^2 for TTB_A and 9(λa)^2 for TTB_O, respectively. Thus, TTB_O associated with $C^I_{1,2}$ TTJ is energetically preferred than TTBA. The similar analysis reveals that TTBA associated with $C^I_{1,4}$TTJs is energetically preferred than TTB_O. The results are in agreement with experimental observation.

5. Conclusion

$\{11\bar{2}2\}$ contraction twins in Ti are frequently generated in rolled pure titanium. The double twinning ($\{10\bar{1}2\}$ extension twins in $\{11\bar{2}2\}$ contraction twins) and $\{11\bar{2}2\}$ twin–twin interactions commonly take place and affect strain hardening rate. Here, we conduct statistical analysis of {1῁22} twin–twin junctions and characterise structural features of {1῁22} TTJs. Corresponding to the crystallography of {1῁22} twins, three types of {1῁22} TTJs form, Type I $C^I_{i,j+1}$, Type II $C^I_{i,j+2}$, and Type III $C^I_{i,j+3}$. Type III $C^I_{i,j+3}$ is associated with the interaction of two con-zone variants. EBSD analysis reveals that type I $C^I_{i,j+1}$TTJs are the most popular among three types of TTJs while type III $C^I_{i,j+3}$TTJs are rare. According the generalised SF analysis, no twin transmission happens, instead, twin–twin boundaries form. Schmid factor analysis for all detected TTJs indicates that the SFs of two twins associated with 93% detected TTJs are first, second, or third highest among six variants. Such information enables us to explore the frequency of forming each type of TTJs. The result clearly demonstrates that the formation of Type I TTJs should be the most popular, while Type III TTJs should be rarely activated. This is in agreement with experimental observations. Consequently, twin transmission across another twin is mechanically unfavourable due to the small resolved shear

stress. Thus, twin–twin junctions form. The interesting is that TTBs only form in one side of the incoming twin. Based on the interactions of twinning dislocations, interface dislocations in the observed TTBs have lower line energy. These structural characters of TTJs and corresponding mechanics will provide insights for developing meso/macro-scale crystal plasticity models of hexagonal metals [44–46]. Finally, it is noted that structural features is characterised in this work based on crystallography, EBSD characterisations and dislocation theory at meso/macro-scales, atomic-level structures are lack. Future work will focus on characterising atomic structures of TTBs and understanding the influence of TTBs on secondary twinning and consequent twinning and detwinning events using atomistic simulations and transmission electron microscopes.

Acknowledgements

M.Y. Gong, X.Y. Xie and J. Wang acknowledge the support from the US National Science Foundation (NSF-CMMI-1661686). S. Xu thanks the Ministry of National Education, Higher Education and Research of France for providing the Doctoral Contract.

Disclosure statement

No potential conflict of interest was reported by the authors.

References

[1] B. Hanson, Mater. Des. 7 (1986) p.301.

[2] L. Jiang, J.J. Jonas, R. Mishra, A. Luo, A. Sachdev and S. Godet, Acta Mater. 55 (2007) p.3899.

[3] C. Cepeda-Jiménez, J. Molina-Aldareguia and M. Pérez-Prado, Acta Mater. 88 (2015) p.232.

[4] J. del Valle, F. Carreño and O.A. Ruano, Acta Mater. 54 (2006) p.4247.

[5] H. Wang, P. Wu and J. Wang, Int. J. Plast. 47 (2013) p.49.

[6] L. Wu, S. Agnew, D. Brown, G. Stoica, B. Clausen, A. Jain, D. Fielden and P. Liaw, Acta Mater. 56 (2008) p.3699.

[7] G. Proust, C.N. Tomé, A. Jain and S.R. Agnew, Int. J. Plast. 25 (2009) p.861.

[8] S. Agnew, M. Yoo and C. Tome, Acta Mater. 49 (2001) p.4277.

[9] T. Al-Samman and X. Li, Mater. Sci. Eng. A 528 (2011) p.3809.

[10] J. Bohlen, M.R. Nürnberg, J.W. Senn, D. Letzig and S.R. Agnew, Acta Mater. 55 (2007) p.2101.

[11] C. Cepeda-Jiménez, J. Molina-Aldareguia and M. Pérez-Prado, Acta Mater. 84 (2015) p.443.

[12] J.T. Wang, J.Q. Liu, J. Tao, Y.L. Su and X. Zhao, Scr. Mater. 59 (2008) p.63.

[13] B.-Y. Liu, J. Wang, B. Li, L. Lu, X.-Y. Zhang, Z.-W. Shan, J. Li, C.-L. Jia, J. Sun and E. Ma, Nat. Commun. 5 (2014).p.3297.

[14] Q. Yu, Z.-W. Shan, J. Li, X. Huang, L. Xiao, J. Sun and E. Ma, Nature 463 (2010) p.335.

[15] S. Sinha, A. Ghosh and N. Gurao, Philos. Mag. 96 (2016) p.1485.

[16] N. Gurao, R. Kapoor and S. Suwas, Acta Mater. 59 (2011) p.3431.

[17] T. Bieler, P. Eisenlohr, C. Zhang, H. Phukan and M. Crimp, Curr. Opin. Solid State Mater. Sci. 18 (2014) p.212.

[18] A.A. Salem, S.R. Kalidindi and R.D. Doherty, Acta Mater. 51 (2003) p.4225.

[19] L. Wang, P. Eisenlohr, Y. Yang, T. Bieler and M. Crimp, Scr. Mater. 63 (2010) p.827.

[20] L. Capolungo and I. Beyerlein, Phys. Rev. B 78 (2008) p.024117.

[21] S. Jin, K. Marthinsen and Y. Li, Acta Mater. 120 (2016) p.403.

[22] L. Wang, R. Barabash, T. Bieler, W. Liu and P. Eisenlohr, Metall. Mater. Trans. A 44 (2013) p.3664.

[23] S. Xu, M. Gong, C. Schuman, J.-S. Lecomte, X. Xie and J. Wang, Acta Mater. 132 (2017) p.57.

[24] S. Wang, Y. Zhang, C. Schuman, J.-S. Lecomte, X. Zhao, L. Zuo, M.-J. Philippe and C. Esling, Acta Mater. 82 (2015) p.424.

[25] S.J. Lainé and K.M. Knowles, Philos. Mag. 95 (2015) p.2153.

[26] F. Xu, X. Zhang, H. Ni and Q. Liu, Mater. Sci. Eng. A 541 (2012) p.190.

[27] Y. Li, Y. Chen, J. Walmsley, R. Mathinsen, S. Dumoulin and H. Roven, Scr. Mater. 62 (2010) p.443.

[28] S. Xu, C. Schuman and J.-S. Lecomte, Scr. Mater. 116 (2016) p.152.

[29] N. Bozzolo, L. Chan and A.D. Rollett, J. Appl. Crystallogr. 43 (2010) p.596.

[30] S. Mullins and B. Patchett, Metall. Trans. A 12 (1981) p.853.

[31] W. Tirry, S. Bouvier, N. Benmhenni, W. Hammami, A. Habraken, F. Coghe, D. Schryvers and L. Rabet, Mater. Charact. 72 (2012) p.24.

[32] A. Serra, D. Bacon and R. Pond, Acta Metall. 36 (1988) p.3183.

[33] B. Morrow, R. Lebensohn, C. Trujillo, D. Martinez, F. Addessio, C. Bronkhorst, T. Lookman and E. Cerreta, Int. J. Plast. 82 (2016) p.225.

[34] A.A. Salem, S.R. Kalidindi and R.D. Doherty, Scr. Mater. 46 (2002) p.419.

[35] S. Xu, L.S. Toth, C. Schuman, J.-S. Lecomte and M.R. Barnett, Acta Mater. 124 (2017) p.59.

[36] Q. Yu, J. Wang, Y. Jiang, R.J. McCabe, N. Li and C.N. Tomé, Acta Mater. 77 (2014) p.28.

[37] Q. Yu, J. Wang, Y. Jiang, R.J. McCabe and C.N. Tomé, Mater. Res. Lett. 2 (2013) p.82.

[38] Q. Sun, X. Zhang, Y. Ren, L. Tan and J. Tu, Mater. Charact. 109 (2015) p.160.

[39] E. Roberts and P. Partridge, Acta Metall. 14 (1966) p.513.

[40] J. Wang and I.J. Beyerlein, Model. Simul. Mater. Sci. Eng. 20 (2012) p.024002.

[41] J. Wang and I.J. Beyerlein, Metall. Mater. Trans. A 43 (2012) p.3556.

[42] M. Gong, J.P. Hirth, Y. Liu, Y. Shen and J. Wang, Mater. Res. Lett. (2017) p.1.

[43] J.P. Hirth and J. Lothe, Theory of dislocations, McGraw-Hill, New York, 1968.

[44] H. Qiao, S. Agnew and P. Wu, Int. J. Plast. 65 (2015) p.61.

[45] H. Qiao, M. Barnett and P. Wu, Int. J. Plast. 86 (2016) p.70.

[46] H. Wang, P. Wu and J. Wang, Comput. Mater. Sci. 96 (2015) p.214.